CuO–TiO_2 based self-powered broad band photodetector

Chiranjib Ghosh [a,1], Arka Dey [a,*,1], Iman Biswas [a], Rajeev Kumar Gupta [b], Vikram Singh Yadav [c], Ashish Yadav [d], Neha Yadav [d], Hongyu Zheng [d], Mohamed Henini [e], Aniruddha Mondal [a,**]

[a] *Department of Physics, National Institute of Technology Durgapur, West Bengal, India*
[b] *Department of Physics, University of Petroleum & Energy Studies Dehradun, Uttarakhand, India*
[c] *Babasaheb Bhimrao Ambedkar University, Lucknow, 226031, India*
[d] *Center for Advanced Laser Manufacturing (CALM), Shandong University of Technology, Zibo, 255000, PR China*
[e] *School of Physics and Astronomy, University of Nottingham, Nottingham, NG7 2RD, United Kingdom*

Keywords: Self-powered CuO–TiO_2 nanocomposite
Broadband photodetector
Two-zone horizontal tube furnace Responsivity

ABSTRACT

An efficient room-temperature self-powered, broadband (300 nm–1100 nm) photodetector based on a CuO–TiO_2/TiO_2/p-Si(100) heterostructure is demonstrated. The CuO–TiO_2 nanocomposites were grown in a two-zone horizontal tube furnace on a 40 nm TiO_2 thin film deposited on a p-type Si(100) substrate. The CuO–TiO_2/ TiO_2/p-Si(100) devices exhibited excellent rectification characteristics under dark and individual photo-illumination conditions. The devices showed remarkable photo-response under broadband (300–1100 nm) light illumination at zero bias voltage, indicating the achievement of highly sensitive self-powered photodetectors at visible and near-infrared light illuminations. The maximum response of the devices is observed at 300 nm for an illumination power of 10 W. The response and recovery times were calculated as 86 ms and 78 ms, respectively. Moreover, under a small bias, the devices showed a prompt binary response by altering the current from positive to negative under illumination conditions. The main reason behind this binary response is the low turn-on voltage and photovoltaic characteristics of the devices. Under illumination conditions, the generation of photo-current is due to the separation of photogenerated electron-hole pairs within the built-in electric field at the CuO–TiO_2/TiO_2 interface. These characteristics make the CuO–TiO_2/TiO_2 broadband photodetectors suitable for applications that require high response speeds and self-sufficient functionality.

1. Introduction

The common view on nanosystems in recent years is functional applications. The requirements of systems must not only consist of communication proficiencies, better control, enhanced catalytic activity, and good sensing properties but must also include self-sufficiency [1,2]. For example, for any field of application a self-driven nanoscale photodetector must be a low cost user-friendly with high sensitivity and response speed [3]. A photodetector has become an essential semiconductor device owing to its applicability in various day-to-day life appliances like compact smoke detectors, disk players, remote control, etc. Recently photodetectors have gained more attention due to their sophisticated usefulness in the field of optical communication, space research, and environmental monitoring [4]. In addition, the broadband (visible-infrared region) photodetectors play a major role in the field of biological and environmental research as well as for imaging, chemical analysis, and communications [5–8]. There are different types of photodetectors depending of the detection mechanisms. These include photodiode, photo-electrochemistry, and photoconduction action [9,10]. For better detectivity most photodetectors require an external bias, which is a constant electrical power source. Therefore, this makes the circuitry of the system heavy and unprofitable in the application field of energy devices. To make it hassle-free, the self-powered photodetector was introduced which can operate without any power source applied externally, i.e. zero-voltage bias. Till now, many photovoltaic effect-based photodetectors have already been reported [11,12]. Owing to the inherent built-in electric field in heterojunctions, Schottky diodes, and organic/inorganic hybrid junctions, the photodetectors based on these systems can operate at zero bias because they can instantly split up the generated electron-hole pairs. This results in faster photoresponse

* Corresponding author.
** Corresponding author.
E-mail addresses: arka.dey2021@gmail.com (A. Dey), aniruddhamo@gmail.com (A. Mondal).

1

and great responsivity at zero bias, which make these photodetectors popular among scientists as well as technologists [13]. Under nominal zero applied bias or short-circuit conditions, the broadband photodetectors are workable. At this zero-bias operating condition, Schottky diodes or p-n heterojunctions can be used [14]. The broadband photodetector covers several passbands, which allows a large bandwidth over a single medium and this is its main advantage for many applications. On the other hand, due to the high surface-to-volume ratio and low reflectance, nanostructured materials offer advantageous high sensitivity, low energy consumption, and high response speed. In nano-structured materials, low reflectance enhances photon collection efficiency and low dimensions decrease the transit times of the carriers by minimizing the effective conductive channels [15,16]. Therefor, nano-structured self-powered broadband detectors that have a high response in weak light conditions with great photosensitivity will be very promising in the application field of future nano-optoelectronic integrated circuits, and radiation resistance environment [17]. However, it remains a very challenging task to fabricate such devices on a nanoscale. Nano-sized transition metal oxides, as well as cupric oxide (CuO) and titanium oxide (TiO_2), are the subject of attractive scientific interest, due to their potential use in catalysis, sensing, cosmetics, biomedical field, enhanced photocatalytic performance, optoelectronic devices, and magnetism [18–21]. CuO, which is a p-type semiconductor with a narrow badngap (1.2–1.35 eV) and photoconductive and photochemical characteristics, has found applications in gas sensing [22], catalysis [23,24], as an antimicrobial agent [25], batteries [26], magnetic devices [27,28], supercapacitors [29], and field emission devices [30]. On the other hand, TiO_2 is a well-known new generation, wide-bandgap (3.2 eV–3.6 eV) n-type semiconductor. TiO_2 has wide applicability in the field of paper, cosmetics, medical device coating [31], and gas sensors [22]. Furthermore, titanium dioxide (TiO_2) emerges as an exceptionally compelling material choice for the development of high-performance UV photodetectors, owing to its exceptional attributes. These include a low permittivity, remarkable resistance to high electric-field breakdowns, commendable thermal conductivity, rapid electron saturation rates, superior radiation resilience, and a well-suited spectral range for effective UV responsiveness [32,33]. The photoelectric conversion mechanisms within semiconductor-based photodetectors can be broadly delineated through an examination of the behaviours exhibited by charge carriers. This includes their generation, separation, transportation, and eventual extraction [32]. Consequently, any factor that exerts an influence on the behaviours of photon-generated carriers becomes a pivotal parameter for fine-tuning and enhancing their photodetection capabilities. The easiness of formation of a heterojunction by reaction with another material is the advantageous characteristic of TiO_2 [34]. The important parameter for the application in the field of optoelectronics is the specific surface area, which is strongly inlaid with the nanostructured morphology. Some material properties may become prominent and change or get enhanced from those of the bulk material when its size decreases to the nanometre scale. Some properties of both TiO_2 and CuO depend on their microstructure, such as the size and morphology, and alignment of the crystal grains. The unique properties of composite nanomaterials propagate from their capacity to combine the most elegant physicochemical features of their elements. CuO–TiO_2 nanocomposite is such a composite material that has great attraction due to its stability, narrow bandgap, easy availability, and nontoxicity [35–37].

This comprehensive report details our intricate process of depositing nanocomposites (NCs) comprised of CuO–TiO_2, meticulously synthesized from a blend of CuO and TiO_2 powders within a state-of-the-art two-zone horizontal tube furnace. The fabrication of our cutting-edge photode-tector device was executed on a meticulously prepared p-Si substrate, a crucial foundation for its subsequent performance. We have begun by providing an in-depth exploration of the fundamental structural and optical characteristics inherent to CuO–TiO_2 NCs. This foundational knowledge serves as a cornerstone for comprehending and, importantly, fine-tuning the photoelectric capabilities of our device. Our report subsequently delves into the remarkable performance of this device, highlighting its unique attributes as a self-powered detector capable of responding to a broad spectrum spanning from 300 to 1100 nm, all achieved at zero bias. As we shift our focus towards the photodetector's response characteristics, a captivating narrative unfolds. Our meticulously constructed CuO–TiO_2 nanocomposites/TiO_2 thin film heterostructure photodetector exhibits an impressive rapid response, boasting a mere 86 ms rise time and a swift 78 ms recovery time. These values underscore the innate agility of our photodetector, swiftly reacting to incoming light stimuli with remarkable precision. Furthermore, under a slight forward bias, our photodetector reveals its prowess by demonstrating a binary response to broad-spectrum light, thereby showcasing its exceptional speed and precision in a range of operational conditions.

2. Experimental details *2.1.*

Deposition of TiO_2 thin films

Using the e-beam evaporation technique (BC-300, Hind High Vacuum, India) and maintaining a base pressure at 5×10^{-6} mbar, a ~40 nm thick TiO_2 thin film (TF)) was deposited on RCA (Radio Corporation of America) cleaned p-type Si (100) wafers (Tedd Pella, USA, 10-30 Ω-cm). Pellets of TiO_2, which were used as the source material for evaporation, were prepared by mixing TiO_2 powder (99.9 %, Loba Chemie) and Polyvinyl Alcohol (PVA) (PVA was used as a binder) as described elsewhere [31].

2.2. Deposition of CuO–TiO_2 nanocomposites

The CuO–TiO_2 nanocomposites (NCs) were deposited in a two-zone horizontal tube furnace on freshly prepared TiO_2 TF coated p-type Si substrate. Here a mix of TiO_2 and CuO (Merck) powder was used as the source material. The deposition was carried out under a flow of Ar (99.99 % purity) at 200 Standard cubic centimeters per minute (SCCM). Upon reaching a system pressure of $\sim 10^{-3}$ mbar, the gas flow was stopped and the sample was subjected to inductive heating. The source temperature was kept at 950–960 °C to evaporate the mixture of TiO_2 and CuO (1:1) powder. The temperature of the substrate was raised to the growth temperature (T_g) (475–480 °C). The process was carried out for 60 min to obtain CuO–TiO_2 NCs.

2.3. Deposition of plasmonic Ag nanoparticles and Au electrode

The nanoparticles (NPs) of Ag (Merck) were deposited above the freshly prepared TiO_2–CuO NCs in a thermal evaporation unit (Provak) at a base pressure of 2×10^{-5} mbar. The substrate was placed at a distance of 8 cm from the evaporation source and was rotated azimuthally at ~350 rpm for 20 s to grow Ag NPs. The deposition procedure of Ag NPs has been described elsewhere [31]. After the deposition of Ag NPs, metal electrodes consisting of gold (Au) was deposited through a shadow mask in the same thermal evaporation unit to form circular mesas of 0.5 mm radius. A flow chart of device fabrication is shown in Fig. 1.

3. Characterization and measurements

The samples were characterized using an X-ray diffractometer (Rigaku Smartlab Instrument with Cu-K_α radiation source, wavelength = 1.54 Å, Field Emission Scanning Electron Microscopy (FESEM, ZEISS, Sigma), and UV–vis spectrophotometer (PerkinElmer Lambda 365+) with an integrated sphere. The photoelectric characteristics were obtained by using Keithley 2405 source meter under dark and illumination conditions. For electrical characterization at different wavelengths and white illumination, a monochromator (300 W ozone-free Xenon arc lamp) was employed.

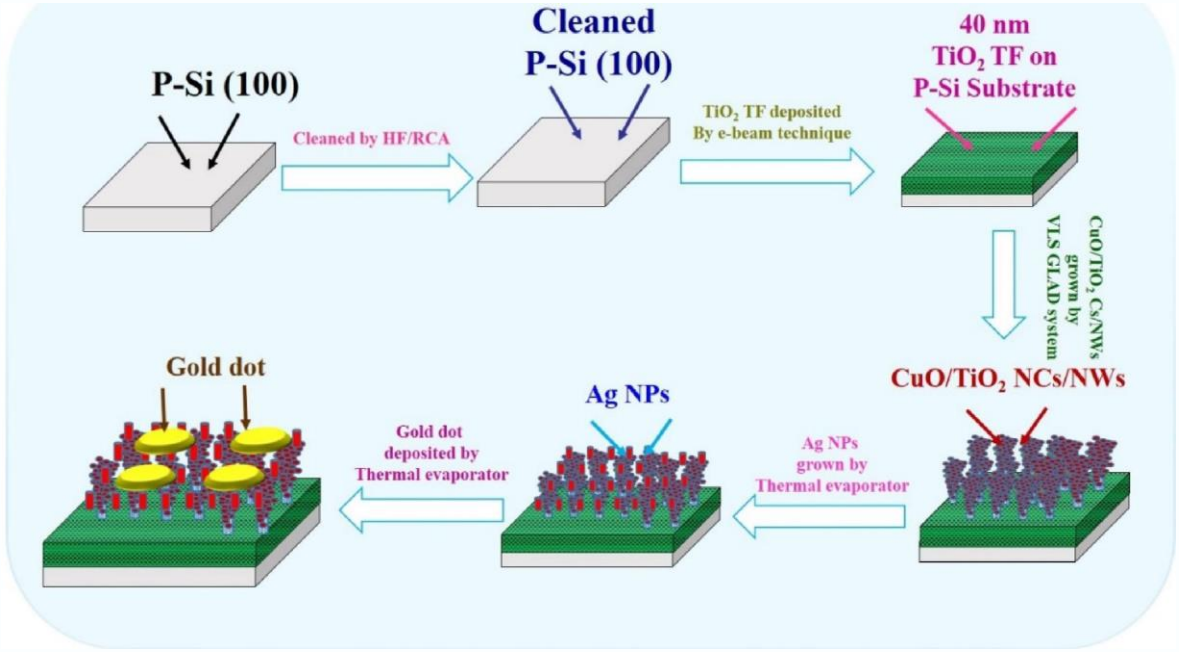

Fig. 1. Flow chart of device fabrication.

4. Results and discussion

4.1. Structural and morphological characterization

The microscopic image (Fig. 2) from the FESEM instrument was used for analyzing the structural morphology of the deposited nanostructure. Inset of Fig. 2 shows the top view of as-grown nanocomposite materials which reveals the formation of clusters of CuO–TiO2 NCs.

The high surface diffusion of the deposited CuO–TiO2 NCs may be the main reason for the formation of such clusters [38,39]. The formation of NC clusters on the substrate may be caused by the high diffusion coefficient that results from the high substrate temperature (T_s = 475 °C–480 °C). The microstructure of the layer grown via physical vapour deposition depends on the ratio of substrate temperature (T_s) and growth temperature (T_g), and categorized as Zone I, II & III [40]. In this work, the ratio between the substrate temperature (T_s = 475 °C–480 °C) and growth temperature (T_g = 970 °C–975 °C) of Ts/Tg = ~0.49, which indicates the growth carried out in Zone III [31]. According to Gall et al. in this Zone III, the microstructure is governed by bulk diffusion, and the microstructure exhibits equiaxed grains [41]. The large diffusion of molecules also enhances the width of the deposited nanocomposites and decreases the aspect ratio of the nanocomposites. Fig. 2 shows the in-depth micrograph of our fabricated heterostructure device where each of layer is indicated with an individual arrow. It represents the successive deposition of TiO2 TFs and CuO–TiO2 NCs on the p-Si(100) substrate.

Fig. 3 shows the XRD pattern of the as-prepared CuO–TiO2 NCs. The resulting nanocomposites possess a high degree of crystalline character, as indicated by the sharp and strong peaks. The structure of the CuO–TiO2 nanocomposites is well supported by the JCPDS Cards Nos. 45–937, 76–1934, 88–1175, and 720639, which also validated the CuO monoclinic and tetragonal TiO2 (rutile and brookite) states of the materials [42,43]. In particular, the patterns showed the reflections peaks at 2θ = 32.44°, 38.72°, 53.40°, and 66.2° which are related to (100), (111), (320), (410) crystal planes, respectively (JCPDS Card No. 45–937). CuO

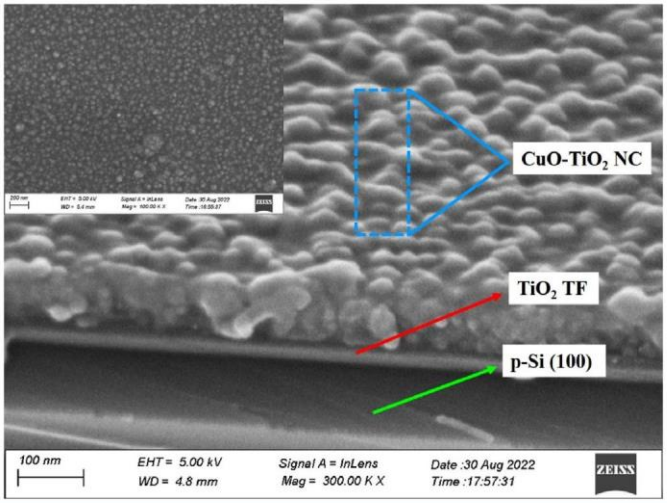

Fig. 2. FESEM image of deposited CuO–TiO2 NCs/TiO2 TF on p-Si Substrate.

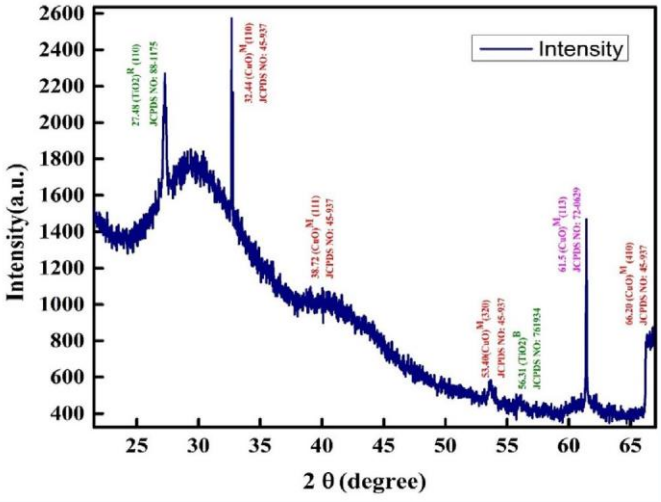

Fig. 3. XRD pattern of CuO–TiO2 nanocomposites.

has a complex monoclinic tenorite crystallographic structure. The obtained peaks at around $2\theta = 27.48^{\circ}$, 56.31° are assigned to the diffraction of the (110) and (412) planes of the TiO_2. The obtained whole diffraction pattern of our sample indicates the coexisting of CuO and TiO_2 as a composite [44].

4.2. Optical characterization

Using the UV–Vis absorption spectra (inset of Fig. 4) the optical direct bandgap (E_g) for CuO–TiO_2 nanocomposites has been calculated. In this regard, Tauc's equation is used [45,46].

$$\alpha h\nu = A(h\nu - E_g)^n \quad (\alpha h\nu) = A(h\nu - E_g)^n$$

where α is absorption coefficient, E_g is the bandgap, h is the Planck's constant, and ν is the frequency of light. n is a constant and depends on the electron transition processes. A is a constant which is considered as 1 for ideal case.

To calculate the direct optical badngap the value of the exponent n in the above equation has been considered as $n = 1/2$ [45,46]. By extrapolating the linear region of the plot ($\alpha h\nu$) [2] *vs.* $h\nu$ (Fig. 4) to $\alpha = 0$ absorption, the value of optical direct bandgap (E_g) has been calculated as 2.86 eV for CuO–TiO_2 nanocomposites. The calculated badngap value of our synthesized composite, which is very different from its constituent materials TiO_2 (~3.2 eV) and CuO (~1.2 eV), confirms the generation of some mixed phase. In other terms, it validates the synthesis of the mixed-phase of CuO–TiO_2 nanomaterials, which has been termed as nanocomposite in this article.

4.3. Electrical characterization

A detailed image of our fabricated CuO–TiO_2 nanocomposite-based device is presented in Fig. 5. Fig. 5a shows the real image of the device. Here we can see the round shape gold (Au) as metal electrodes and was deposited through a shadow mask in the same thermal evaporation unit to form circular mesas of 0.5 mm radius. Fig. 5b represent the corresponding FESEM image of the device, where the substrate and the two different layer of TiO_2 TF, the CuO–TiO_2 NCs are distinguishly visible. Fig. 5c shows schematic diagram of the device. It shows the deposited layer of TiO_2 TF of around ~40 nm thick upon the p-type Si substrate. Upon the active layer of TiO_2 TF, the CuO–TiO_2 NCs were deposited and then the Ag NPs were formed by thermal evaporation technique. Here the gold (Au) was used as metal electrodes.

The typical current-voltage (I–V) characteristic at room temperature of our fabricated device under dark conditions is presented in Fig. 6a. The

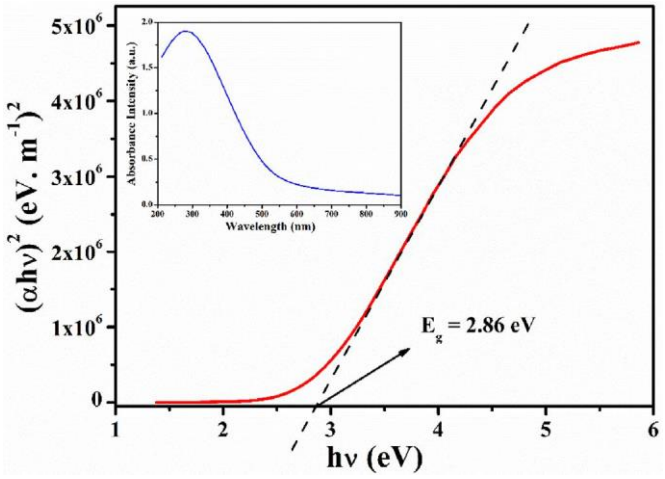

Fig. 4. Optical direct bandgap (E_g) and UV–Vis absorption spectra (inset) of CuO–TiO_2 nanocomposite.

corresponding semilog I–V plot is also given in the inset of Fig. 6a. The results undoubtedly reveal a nonlinear characteristic of our Au/ CuO–TiO_2/TiO_2/p-Si (100) heterojunction device, typical of standard rectifying diodes. The rectification ratio at bias voltages of ±3 V was calculated as 506.69, with the turn-on voltage at ~0.8 V. This rectification behavior must mainly arise from the CuO–TiO_2 NCs/TiO_2 TF contact. The devices were investigated under white light with varying powers. Here we used 10 W, 12 W, 14 W, and 16 W power of the light source to illuminate the devices. Fig. 6b illustrates the room-temperature I–V characteristics under different illumination conditions.

In every illumination (different power) condition, the obtained results clearly exhibit non-linear rectifying characteristics. The rectification ratio of our device gradually increases to 612, 666, 711, and 806 under the gradual increase of power of the incident illumination of 10 W, 12 W, 14 W, and 16 W respectively.

To examine the activity of our devices at various wavelengths, we have measured the I–V characteristics under specific wavelengths, namely 300 nm, 550 nm, 900 nm, and 1100 nm, at a fixed power of illumination of 10 W. Spectral response studies at different wavelengths (λ = 300-1100 nm) at zero bias and constant incident illumination power of 10 W were also carried out. Fig. 7a-e shows the comparison of I–V curves of the CuO–TiO_2 NCs/TiO_2 TF heterojunction devices under dark cand illuminated conditions. In all the I–V curves two significant features can be seen: i) a small but measurable photovoltaic effect was observed when the device was illuminated with light of different wavelengths; ii) in response to the light sources being switched off and on, the electrical current of the photodetector changes from positive to negative (i.e., a binary current phenomenon) when a small forward bias is applied.

The photoresponses of the fabricated devices under a slight forward bias and zero bias subjected to white light and various illumination conditions are shown in Fig. 7 f-j. The reproducibility and good stability of the photoresponse for four cycles of switching are also demonstrated in this figure. The rapid response of the devices can be realized from the sharp rise and fall edges. In addition, from the photoresponse under zero bias the photosensitivity of the photodetectors was obtained. The photosensivities under zero bias at 300 nm, 550 nm, 900 nm, 1100 nm, and white light were 7.13, 15.96, 7.09, 5.35, and 8.09, respectively. The well-organized TiO_2 TF structure and the CuO–TiO_2 NCs assembly can greatly absorb a wide spectral range, from visible to near-infrared. These combined actions at the interface of the TiO_2 TF and the CuO–TiO_2 NCs are the main reason behind the high photosensitivity of the devices. This could provide a high photocurrent and considerably enhance the device's ability in photvoltaic applications. In the meantime, both a high photocurrent and a low dark current (0.087 nA at zero bias) can be achieved due to the generated built-in electric field within the CuO–TiO_2 NCs/ TiO_2 TF junction.

Furthermore, when subjected to a minor forward bias, intriguing variations in current emerge upon the cycling of light at different wavelengths – a transition between positive and negative current states. The intricate current behaviors represented in the I–V characteristics of the devices featured in Fig. 8a–e shed light on the mechanisms underlying this fluctuation, which could potentially elucidate the genesis of the binary response exhibited under the modest forward bias condition. In the absence of external illumination, a slight forward bias yields a positive current in the device, manifesting as a response in a darkened environment. However, when an applied bias is introduced under the influence of light, a photoinduced electromotive force materializes, instigating a reversal of current from positive to negative. This captivating phenomenon presents an enticing prospect, offering the device's utility as an on-off binary response instrument for the expansive realm of broadband photodetection.

The photoresponse of the CuO–TiO_2 NCs-based devices was verified under different irradiance conditions by varying the intensity. For all of the light sources with varying wavelengths, Fig. 8a–e depicts progressively rising photocurrent responses with rising irradiance intensity. For the white light source, the photocurrents increase from 1.65×10^{-10} A to

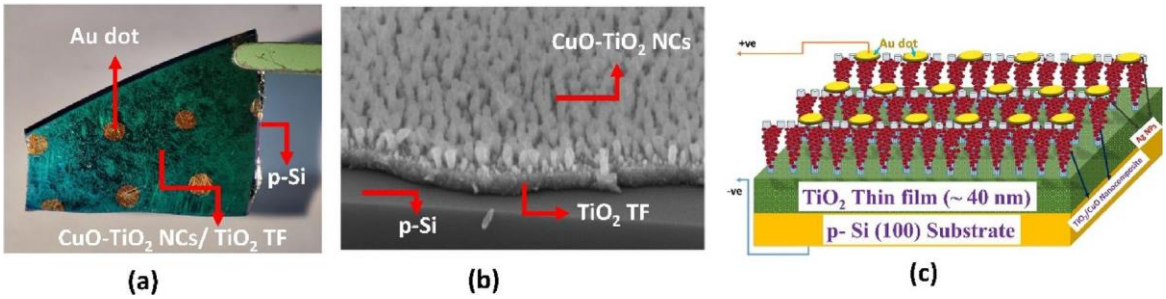

Fig. 5. (a) Real image, (b) Corresponding FESEM image, and (c) Schematic diagram of our device.

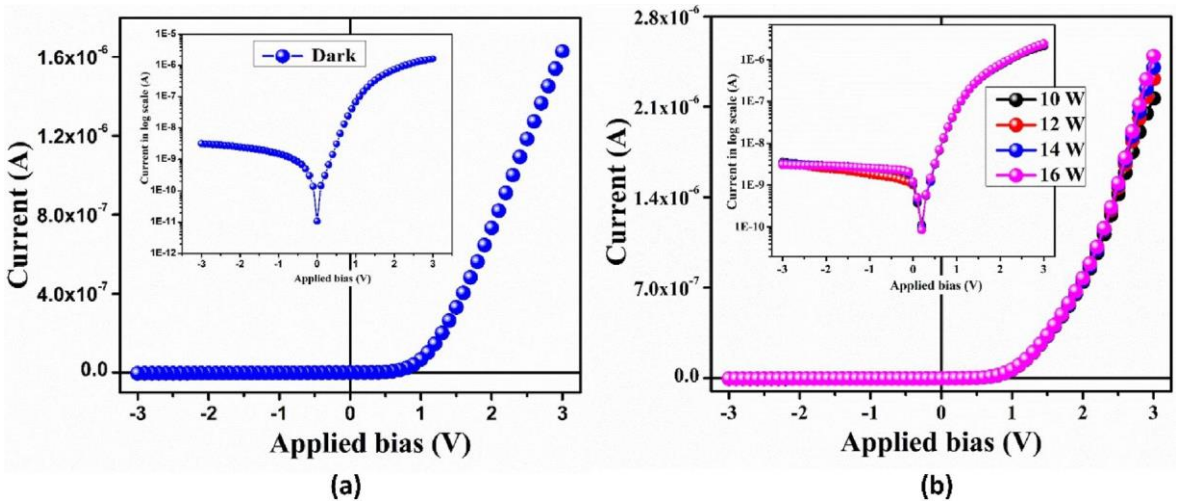

Fig. 6. (a) Linear and semi-logarithmic (inset) plots of I–V in the dark and (b) Linear and semi-logarithmic (inset) plots of I–V characteristics of the device exposed to white light with different powers of the light source.

2.33×10^{-10} A with the increase of irradiance intensities from 10 W to 16 W, respectively. A similar effect was also observed for the different wavelengths of 300 nm, 550 nm, 900 nm, and 1100 nm. We have also examined the dependency of photocurrent on incident power, using the simple power law: $I = AP^{\theta}$, and the results are presented in Fig. 8(f-j). In the above equation, I is the photocurrent, A is a constant at a certain wavelength, P is the power density of the input light, and θ is a parameter associated with the trapping and recombination of photocarriers in photodetectors [47]. Using the above equation, the θ fitted values obtained were 0.822, 0.667, 0.867, 0.855, and 0.726 for the wavelengths of 1100 nm, 900 nm, 550 nm, 300 nm, and white light, respectively. The carrier traps on the surface of the CuO–TiO_2 are probably responsible for this fractional power dependence. The nonunity value of θ explains the complex processes of photogenerated carriers through trapping, recombination, etc. [48]

To analyze the detection performance of the CuO–TiO_2 NCs-based devices, the responsivity (R) and detectivity (D*) parameters were determined. The photocurrent produced per unit of the incident power is referred to as R in this instance. D*, which is usually utilized as a material figure of merit to describe the photoconductor sensitivity, is normalized to the active device area (A) and the equivalent noise bandwidth. To determine R and D*, we have used the following equations,

$$R = \frac{\Delta I}{AP}$$

$$D^{*} = \frac{A^{1/2} R}{(2eI_{dark})^{1/2}}$$

where ΔI represents the difference between the dark current and the current under illumination conditions. A is the active contact area and P is the power density of the incident illumination. Table 1 contains the findings for all parameters. It should be mentioned that the devices had poor detectability and responsivity. This is a general characteristic of self-powered detectors as there is no external electric field to drive the dissociation of the excitons.

However, the self-powered devices would still be able to ensure the ability to detect light irradiation because the separation of the excitons is only caused by the built-in electric field. The wavelength dependent obtained R are shown in Fig. 9b, which shows a broad response of the device from 300 nm to 1100 nm. Additionally, it can be seen that the obtained R and D* values are obviously superior under the illumination at a wavelength of 300 nm compared to 550 nm, 900 nm, and 1100 nm wavelength illuminations. This can be explained as follows: when the CuO–TiO_2 NCs/TiO_2 TF heterojunction was irradiated by 300 nm wavelength illumination, the photoexcitation occurred in both CuO–TiO_2 NCs and TiO_2 TF because the photoenergies of the 300 nm beam (~4.14 eV) is higher than the bandgaps of both CuO–TiO_2 NCs (~2.86 eV) and TiO_2 (~3.2 eV) [18,21,31]. In contrast, when the CuO–TiO_2 NCs/TiO_2 TF heterojunction was irradiated with 550 nm, 900 nm, and 1100 nm illumination wavelengths, photoexcitation cannot occur in the hetero-junction because the photoenergies of 550 nm (~2.25 eV), 900 nm (~1.38 eV) and 100 nm (~1.13 eV) illuminations all have photoenergies lower than the badngap of CuO–TiO_2 NCs and TiO_2 TF.

The response and recovery times of the photo generated current were measured using a mechanical light chopper and a precision source/measure unit (Keithley 2405) (Fig. 9a). The test was carried out with an applied field that was nominally zero. Here, the self-powered

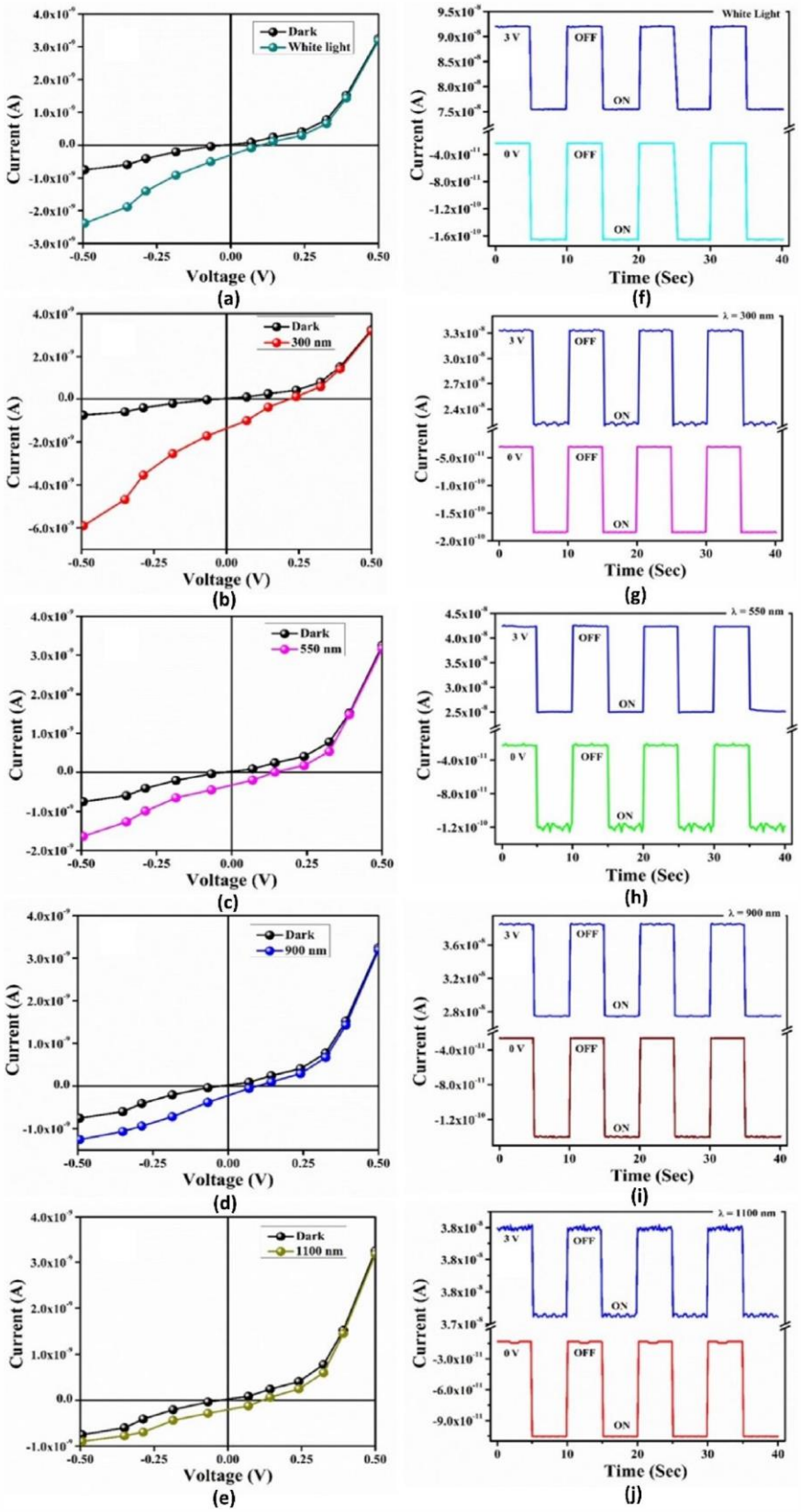

Fig. 7. Photoelectric properties of the CuO/TiO_2 nanocomposites-based devices illuminated at different wavelengths. (a–e) I–V characteristics. (f–j) Photoresponses under zero bias and a small forward bias when irradiation is turned on (5 s) and off (5 s), repeated for four cycles. The light wavelengths are (a, f) white light, (b, g) 300 nm, (c, h) 550 nm, (d, i) 900 nm, and (e, j) 1100 nm.

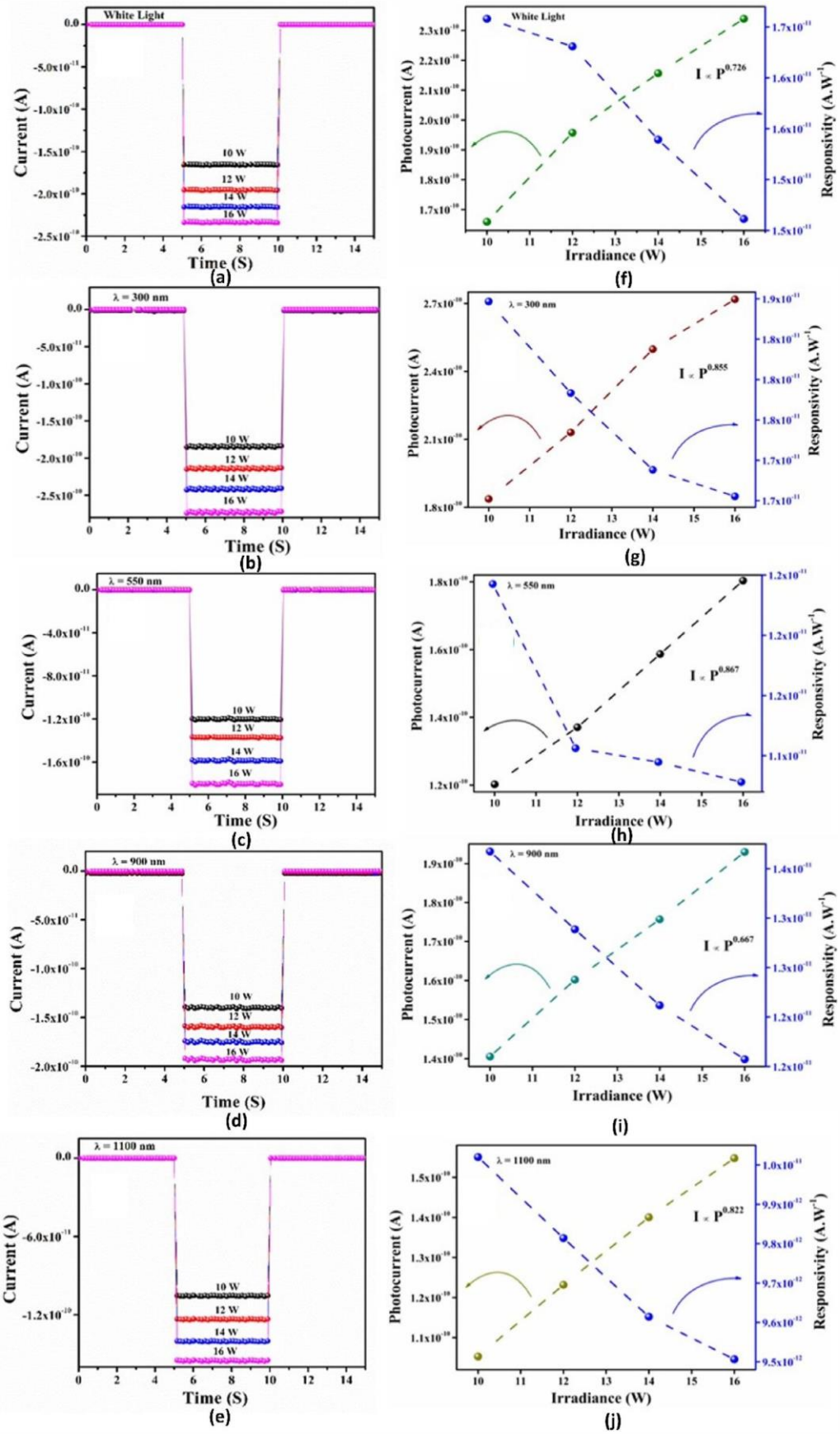

Fig. 8. **(a–e) Photoresponses under zero bias; (f–j) Left Y axis: fitting curves for the relationships between the photocurrent; Right Y axis: device responsivity to illumination at white light and the light source with various intensities for different wavelengths.**

Table 1
Typical photoelectric properties of the CuO–TiO_2 NCs-based photodetector.

Type of Source	Power (W)	Photo Current (A)	Responsivity (A W^{-1})	Detectivity (cm $Hz^{0.5}$ W^{-1})
300 nm	10	-1.836 x 10^{-10}	1.858 x 10^{-11}	2.256 x 10^{6}
550 nm	10	-1.202 x 10^{-10}	1.197 x 10^{-11}	1.453 x 10^{6}
900 nm	10	-1.405 x 10^{-10}	1.374 x 10^{-11}	2.482 x 10^{6}
1100 nm	10	-1.056 x 10^{-10}	1.002 x 10^{-11}	2.634 x 10^{6}
White Light	10	-1.658 x 10^{-10}	1.658 x 10^{-11}	3.142 x 10^{6}

photodetector's temporal photocurrent responses are also shown (Fig. 9a). Within the temporal domain, the photodetector's response is conventionally evaluated through the scrutiny of its temporal characteristics, quantified as the response time (T_{res}). T_{res} delineates the temporal span requisite for ascension from 10 % to 90 % of its zenith intensity. Conversely, the recovery time (T_{rec}) characterizes the interval necessary for the descent from 90 % to 10 % of its maximal output. As delineated in Fig. 9c, a singular, normalized modulation cycle is exhibited. Remarkably, it was ascertained that the response and recovery times approximated 86 and 78 ms, correspondingly. The exceptional expeditiousness in carrier mobility, coupled with the rapid separation of an extensive cohort of photogenerated charge carriers, underpins the remarkable swiftness of this response. This phenomenon is distinctly attributed to the creation of an embedded electric field at the CuO–TiO_2 nanocomposites/TiO_2 thin-film interface. This result suggests that the CuO–TiO_2 NCs/TiO_2 TF heterojunction photodetector can work well as a switching device. Here we compared the calculated values of characteristic parameters of our photodetectors with previously reported values in the literature and presented them in Table 2. From Table 2, it can be seen that the values of responsivity and detectivity of our devices are very low than the reported values. This is a well-known characteristic of self-powered detectors, as there is no external electric field to drive the dissociation of the excitons. It can also be seen that the calculated T_{res} and T_{rec} of our CuO/TiO_2-based devices were found to be better than those of the previously reported values in the literature for CuO and TiO_2-based self-powered photodetectors (Table 2).

We conducted an in-depth analysis of the photovoltaic characteristics of our self-powered CuO–TiO_2 nanocomposites (NCs)/TiO_2 thin film (TF) photodetectors, using an energy band diagram approach (refer to Fig. 10) based on the Anderson-Shockley model, as proposed and illustrated. In this context, "E_g" represents the bandgap of TiO_2 TF (3.20 eV) and CuO–TiO_2 NCs (2.86 eV), while "E_F" denotes the Fermi level. When the CuO–TiO_2 NCs and TiO_2 TF heterojunction forms, the Fermi levels of both materials reach equilibrium, leading to the creation of a depletion region at the interface of the heterojunction. This depletion region generates an inherent electric field at the junction, which in turn induces a bending of the energy bands at the junction [48]. When subjected to white light illumination, it's noteworthy that longer wavelengths are absorbed within the Si/TiO_2 depletion region, leading to a substantial generation of carriers when compared to exposure solely to deep UV light.

Furthermore, the generation of an electrically polarized interface ensues upon the establishment of heterojunctions, as a consequence of a negatively charged silicon (Si) site coalescing with a positively charged titanium dioxide (TiO_2) site at the Si/TiO_2 juncture. This engenders the inception of an intrinsic, embedded electric field, which endures in the absence of any extrinsic bias. Given the non-existence of an external bias in the self-sustaining photodetector, when subjected to white light irradiation, photogenerated electrons seamlessly traverse from the Si to the TiO_2 domain, concurrently with the migration of holes from TiO_2 to Si, each driven by the internal electric field. Moreover, the existence of TiO_2 interposed between the CuO–TiO_2 nanocomposites and Si induces a notable distortion in the energy band structure. There is an upward displacement in energy levels at the CuO–TiO_2 nanocomposites/TiO_2 boundary and a corresponding downward shift at the Si/TiO_2 boundary, leading to a significant band offset. This band offset functions as a compelling impetus for the directed motion of charge carriers towards the electrodes. In this configuration, it is imperative to acknowledge that the photocurrent traverses in the antithetical direction to the dark current, which arises from the diffusion of charge carriers. Consequently, the net device current, denoted as I_{Net}, is mathematically expressed as $I_{Net} = I_{Dark} - I_{Photo}$, and it assumes a negative value since I_{Photo} surpasses I_{Dark}. Thus, the presence of p-type silicon (p-Si) and TiO_2 alongside the CuO–TiO_2 nanocomposites in the device significantly bolsters its functionality across a broad spectrum of incident light wavelengths.

5. Conclusion

In summary, we have fabricated and investigated the photovoltaic characteristics of the self-powered CuO–TiO_2 NCs/TiO_2 TF-based broadband photodetectors. Our fabricated devices showed high photosensitivity and ultrafast response speeds at zero bias under a wide range of photo illumination (300–1100 nm). These devices also demonstrated distinctive binary responses under a small forward bias. These advantages are ascribed to the advantages of the large surface area and the built-in field at the CuO–TiO_2 NCs/TiO_2 junction. The devices can be used as a self-powered photodetector operating at a zero-applied field. The amount of photogenerated carriers in the self-powered hetero-junction devices depends on the generation of photogenerated carriers at the interface, their separation at the interface, and their collection by the electrode. With the simple and easy fabrication procedure, high photosensitivity, self-sufficiency, and good stability, this broadband photode-tector offers a wide range of potential applications in the areas of binary switching, environmental sensing, optoelectronic integrated circuits, and

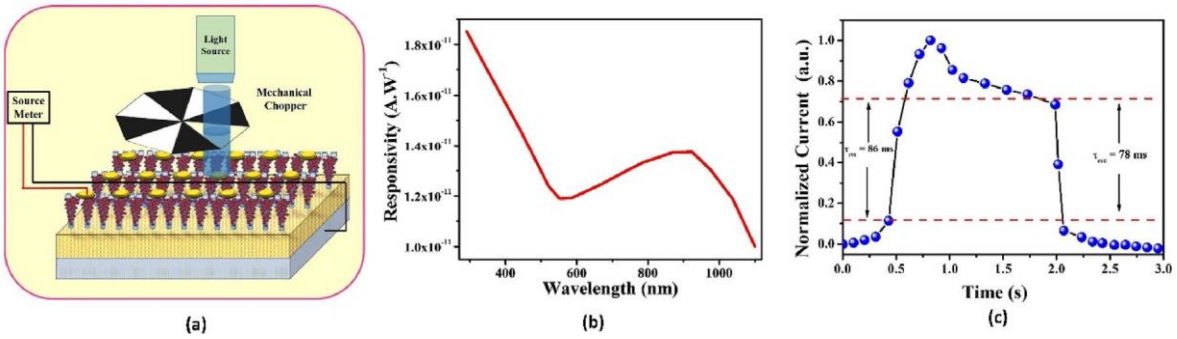

Fig. 9. (a) Schematic diagram for photoresponse measurement arrangement, (b) Wavelength dependend responsivity and (c) Temporal response of the photodetector at zero bias and subjected to white light.

Table 2
Comparison of characteristic parameters of the present CuO/TiO2-based photodetectors with those of other self-powered photodetectors. R = Responsivity, D* = Detectivity, τ_{res} = Response time, τ_{rec} = Recovery time.

Device structure	Type	Wavelength (nm)	R (mA/W)	D* (Jones)	τ_{res} (ms)	τ_{rec} (ms)	Ref.
TiO_2/SnO_2	heterojunction	330	600	–	30	10	[9]
p-CuO/n-ZnO NW	Coaxial nanowire photodiodes	–	0.006	5.37×10^6	1300	1200	[50]
p-CuZnS/n-TiO_2	hybrid heterostructure	300	2.54	–	450	410	[49]
CuO/$In_2Ge_2O_7$	heterojunctions	250	7.34×10^5	–	4200	5200	[51]
SnS_x/TiO_2	heterojunctions	400	5.85	6.54×10^{10}	3	40	[14]
CuI/TiO_2 NRs	heterostructure	410	4.5	1.08×10^{11}	329	220	[17]
Fe:TiO_2/n-Si	heterostructure	350	46	–	10	15	[16]
Ag/CuO NW	heterostructure	540	8	–	15000	17000	[52]
BTO@TO NFs	heterostructure	330	2.56×10^{-2}	2.75×10^7	500	–	[53]
p-CuI/n-TiO_2	heterostructure	260	0.6	8.4×10^{11}	11	72	[54]
Y^{3+}-doped TiO_2 NFMs	heterostructure	350	4.5×10^3	1.6×10^{11}	2530	1160	[55]
Se/TiO_2	p-njunction	620	100	6.2×10^{12}	1.4	7.8	[56]
TiO_2/PC71BM/PEDOT:PSS	heterostructure	350	33	1.6×10^{11}	60	0.001	[57]
CuO–TiO_2 NC/TiO_2 TF	heterostructure	300	1.858×10^{-8}	2.256×10^6	86	78	Present work

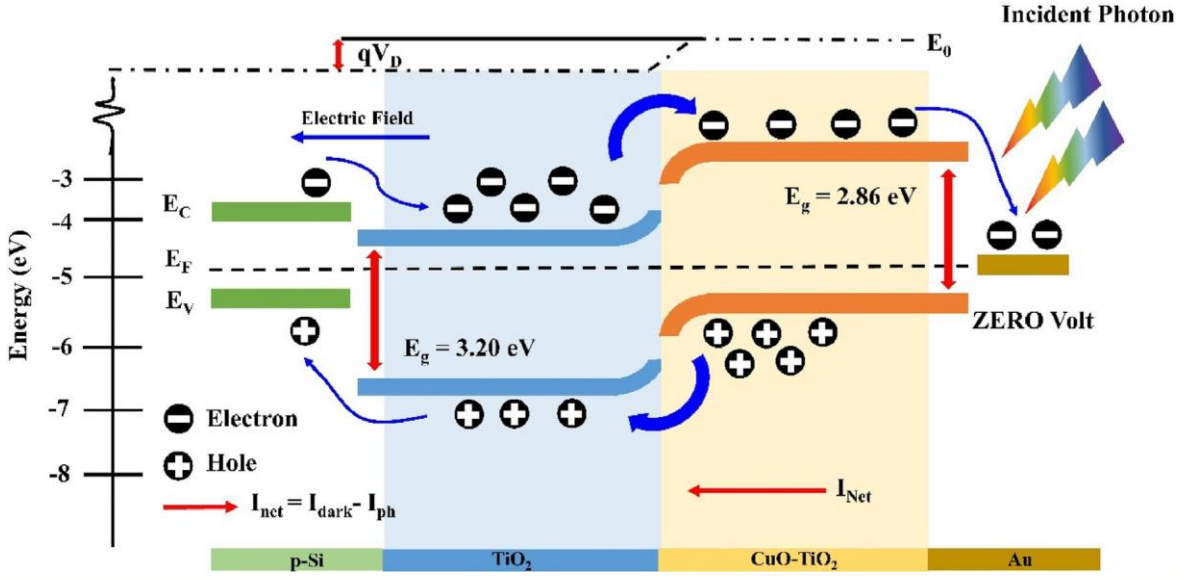

Fig. 10. Energy-band diagram of the CuO–TiO_2 NC/TiO_2 TF heterojunction photodetection under illumination and zero bias conditions.

biosensing. This work delivers a simple and effective way to design an advanced self-powered broadband photodetector. As our devices are responsive not only in the visible range but also in the UV and IR range, it will be suitable for the fabrication of UV and IR photodetectors as an artificial electronic eye which has crucial applications in complex atmospheres and are adaptable to various requirements. We expect our approach would be beneficial for the fabrication of advanced self-powered broadband photodetector integrated on auto-generated power platforms, even multifunctional systems, and smart devices. The excellent performance of the CuO–TiO2/TiO2/p-Si-based self-powered broadband photodetectors will enable momentous progressions for next-generation photodetection and photosensing applications.

Declaration of competing interest

The authors declare that they have no known competing financial interests or personal relationships that could have appeared to influence the work reported in this paper.

Acknowledgments

For financial assistance, the authors thank CSIR- 09/0973(11599)/ 2021-EMR-I and SERB (Project no: CRG/2021/000255), Department of Science and Technology, Govt. of India. The gratefully acknowledge SAIF IIT Bombay for providing the XRD measurements. The COE at NIT Dur-gapur provided the authors with the FESEM facility, which they would like to acknowledge.

References

[1] P. Lin, X. Yan, Z. Zhang, Y. Shen, Y. Zhao, Z. Bai, Y. Zhang, ACS Appl. Mater. Interfaces 5 (2013) 3671–3676, https://doi.org/10.1021/am4008775.
[2] X. Lin, H. Deng, Y. Jia, Z. Wu, Y. Xia, X. Wang, S. Chen, Y. Cheng, Q. Zheng, Y. Lai, S. Cheng, ACS Appl. Mater. Interfaces 14 (2022) 12385–12394, https://doi.org/ 10.1021/acsami.1c25256.
[3] K. Shen, H. Xu, X. Li, J. Guo, S. Sathasivam, M. Wang, A. Ren, K.L. Choy, I.P. Parkin, Z. Guo, J. Wu, Adv. Mater. 32 (2020) 2000004, https://doi.org/10.1002/adma.202000004.
[4] O. Game, U. Singh, T. Kumari, A. Banpurkar, S. Ogale, Nanoscale 6 (2014) 503–513, https://doi.org/10.1039/C3NR04727J.
[5] L. Hu, L. Zhu, H. He, Y. Guo, G. Pan, J. Jiang, Y. Jin, L. Sun, Z. Ye, Nanoscale 5 (2013) 9577–9581, https://doi.org/10.1039/C3NR01979A.
[6] M. Peng, Y. Liu, A. Yu, Y. Zhang, C. Liu, J. Liu, W. Wu, K. Zhang, X. Shi, J. Kou, J. Zhai, Z.L. Wang, ACS Nano 10 (2016) 1572–1579, https://doi.org/10.1021/ acsnano.5b07217.
[7] Q. Zheng, M. Peng, Z. Liu, S. Li, R. Han, H. Ouyang, Y. Fan, C. Pan, W. Hu, J. Zhal, Z. Li, Z.L. Wang, Sci. Adv. 7 (2021) eabe7738.
[8] P. Guo, M. Jia, D. Guo, Z. L. Wang, J. Zhai, https://doi.org/10.1016/j.matt.2022.11.022.
[9] X. Li, C. Gao, H. Duan, B. Lu, Y. Wang, L. Chen, Z. Zhang, X. Pan, E. Xie, Small 9 (2013) 2005–2011, https://doi.org/10.1002/smll.201202408.

[10] G. Konstantatos, E.H. Sargent, Nat. Nanotechnol. 5 (2010) 391–400, https:// doi.org/10.1038/nnano.2010.78.
[11] L. Wang, J. Jie, Z. Shao, Q. Zhang, X. Zhang, Y. Wang, Z. Sun, S.T. Lee, Adv. Funct. Mater. 25 (2015) 2910–2919, https://doi.org/10.1002/adfm.201500216.
[12] W. Ouyang, F. Teng, X. Fang, Adv. Funct. Mater. 28 (2018) 1707178, https:// doi.org/10.1002/adfm.201707178.
[13] P. Yu, K. Hu, H. Chen, L. Zheng, X. Fang, Adv. Funct. Mater. 27 (2017) 1703166, https://doi.org/10.1002/adfm.201703166.
[14] J. Chen, J. Xu, S. Shi, R. Cao, D. Liu, Y. Bu, P. Yang, J. Xu, X. Zhang, L. Li, ACS Appl. Mater. Interfaces 12 (2020) 23145–23154, https://doi.org/10.1021/acsami.0c05247.
[15] A. Srivastava, R. Singh, S. Jit, S. Tripathi, IEEE Electron. Device Lett. 42 (2021) 875–878, https://doi.org/10.1109/LED.2021.3075345.
[16] L. Sun, C. Wang, T. Ji, J. Wang, G.C. Yi, X. Chen, RSC Adv. 7 (2017) 51744–51749, https://doi.org/10.1039/C7RA10439A.
[17] Z. Zhou, X. Li, F. Zhao, C. Wang, M. Zhang, S. He, Y. Zhang, D. Zhang, M. Xu, L. Zhang, Opt. Mater. Express 12 (2022) 392–402, https://doi.org/10.1364/OME.448435.
[18] H. Hamad, M.M. Elsenety, W. Sadik, A.G. El-Demerdash, A. Nashed, A. Mostafa, S. Elyamny, Sci. Rep. 12 (2022) 1–20, https://doi.org/10.1038/s41598-022-05981-7.
[19] M. Diab, B. Moshofsky, I. Jen-La Plante, T. Mokari, J. Mater. Chem. 21 (31) (2011) 11626–11630, https://doi.org/10.1039/C1JM10638D.
[20] R.S. Devan, R.A. Patil, J.H. Lin, Y.R. Ma, Adv. Funct. Mater. 22 (2012) 3326–3370, https://doi.org/10.1002/adfm.201201008.
[21] E.P. Etape, L.J. Ngolui, J. Foba-Tendo, D.M. Yufanyi, B.V. Namondo, J. Appl. Chem. 2017 (2017) 1–10, https://doi.org/10.1155/2017/4518654.
[22] C. Yang, X. Su, J. Wang, X. Cao, S. Wang, L. Zhang, Sensor. Actuator. B Chem. 185 (2013) 159–165, https://doi.org/10.1016/j.snb.2013.04.100.
[23] N. Scotti, D. Monticelli, F. Zaccheria, Inorg. Chim. Acta. 380 (2012) 194–200, https://doi.org/10.1016/j.ica.2011.10.001.
[24] Y. Zhao, X. Song, Z. Yin, Q. Song, J. Colloid Interface Sci. 396 (2013) 29–38, https://doi.org/10.1016/j.jcis.2012.12.071.
[25] M.S. Hassan, T. Amna, O.B. Yang, M.H. El-Newehy, S.S. Al-Deyab, M.S. Khil, Colloids Surf. B Biointerfaces 97 (2012) 201–206, https://doi.org/10.1016/j.colsurfb.2012.04.032.
[26] O. Waser, M. Hess, A. Güntner, P. Novak, S.E. Pratsinis, J. Power Sources 241 (2013) 415–422, https://doi.org/10.1016/j.jpowsour.2013.04.147.
[27] D. Gao, J. Zhang, J. Zhu, J. Qi, Z. Zhang, W. Sui, H. Shi, D. Xue, Nanoscale Res. Lett. 5 (2010) 769–772, https://doi.org/10.1007/s11671-010-9555-8.
[28] T. Ahmad, R. Chopra, K.V. Ramanujachary, S.E. Lofland, A.K. Ganguli, Solid State Sci. 7 (2005) 891–895, https://doi.org/10.1016/j.solidstatesciences.2004.11.029.
[29] A. Pendashteh, M.F. Mousavi, M.S. Rahmanifar, Electrochim. Acta 88 (2013) 347–357, https://doi.org/10.1016/j.electacta.2012.10.088.
[30] Y.W. Zhu, T. Yu, F.C. Cheong, X.J. Xu, C.T. Lim, V.B.C. Tan, J.T.L. Thong, C.H. Sow, Nanotechnology 16 (2004) 88, https://doi.org/10.1088/0957-4484/16/1/018.
[31] C. Ghosh, S.M.M. Dhar Dwivedi, A. Ghosh, A. Dalal, A. Mondal, Appl. Phys. A 125 (2019) 1–9, https://doi.org/10.1007/s00339-019-3108-5.
[32] Z. Li, Z. Li, C. Zuo, X. Fang, Adv. Mater. 34 (2022) 2109083, https://doi.org/ 10.1002/adma.202109083.
[33] Z. Li, T. Yan, X. Fang, Nat. Rev. Mater. 8 (2023) 587–603, https://doi.org/10.1038/s41578-023-00583-9.
[34] C.H. Ashok, V.K. Rao, C.H. Shilpa Chakra, J. Nanomater. Mol. Nanotech. 5 (2016) 12–15, https://doi.org/10.4172/2324-8777.1000178.
[35] L. Dong, H. Chu, X. Wang, Y. Li, S. Zhao, D. Li, Nanophotonics 10 (2021) 1541–1551, https://doi.org/10.1515/nanoph-2020-0649.
[36] M.S.P. Francisco, V.R. Mastelaro, Chem. Mater. 14 (2002) 2514–2518, https://doi.org/10.1021/cm011520b.
[37] Z.K. Heiba, M.B. Mohamed, A.J. Badawi, Inorg. Organomet. Polym. Mater. (2022) 1–10, https://doi.org/10.1007/s10904-022-02312-1.
[38] Z. Liu, C. Zhou, Prog. Nat. Sci.: Mater. Int. 25 (2015) 334–341, https://doi.org/10.1016/j.pnsc.2015.07.005.
[39] J. Banas-Gac, M. Radecka, A. Czapla, E. Kusior, K. Zakrzewska, Appl. Surf. Sci. 616 (2023) 156394, https://doi.org/10.1016/j.apsusc.2023.156394.
[40] J.A. Thornton, J. Vac. Sci. Technol. A 11 (1974) 666, https://doi.org/10.1116/1.1312732.
[41] S. Mukherjee, D. Gall, Thin Solid Films 527 (2013) 158–163, https://doi.org/10.1016/j.tsf.2012.11.007.
[42] K.M.R. Karim, M.A.P. Jebi, H.R. Ong, H. Abdullah, M. Tarek, C.K. Cheng, M.M.R. Khan, In Natl. Conf. Postgrad. Res. (2018) 103–111.
[43] K. Osako, K. Matsuzaki, H. Hosono, G. Yin, D. Atarashi, E. Sakai, T. Susaki, M. Miyauchi, Apl. Mater. 3 (2015) 104409, https://doi.org/10.1063/1.4926934.
[44] N. Boutaleb, F.Z. Dahou, H. Djelad, L. Sabantina, I. Moulefera, A. Benyoucef, Polymers 14 (21) (2022) 4562, https://doi.org/10.3390/polym14214562.
[45] A. Dey, S. Middya, R. Jana, M. Das, J. Datta, A. Layek, P.P. Ray, J. Mater. Sci. Mater. Electron. 27 (2016) 6325–6335, https://doi.org/10.1007/s10854-016-4567-5.
[46] A. Dey, A. Layek, A. Roychowdhury, M. Das, J. Datta, S. Middya, D. Das, P.P. Ray, RSC Adv. 5 (2015) 36560–36567, https://doi.org/10.1039/C4RA16828C.
[47] D. Wu, Y. Jiang, Y. Zhang, J. Li, Y. Yu, Y. Zhang, Z. Zhu, L. Wang, C. Wu, L. Luo, J. Jie, J. Mater. Chem. 22 (2012) 6206–6212, https://doi.org/10.1039/C2JM16632A.
[48] S. Krishna, A. Sharma, N. Aggarwal, S. Husale, G. Gupta, Sol. Energy Mater. Sol. Cell. 172 (2017) 376–383, https://doi.org/10.1016/j.solmat.2017.08.017.
[49] X. Xu, J. Chen, S. Cai, Z. Long, Y. Zhang, L. Su, S. He, C. Tang, P. Liu, H. Peng, X. Fang, Adv. Mater. 30 (2018) 1803165, https://doi.org/10.1002/adma.201803165.
[50] H.T. Hsueh, S.J. Chang, W.Y. Weng, C.L. Hsu, T.J. Hsueh, F.Y. Hung, S.L. Wu, B.T. Dai, IEEE Trans. Nanotechnol. 11 (2012) 127–133, https://doi.org/10.1109/TNANO.2011.2159620.
[51] W. Tian, C. Zhi, T. Zhai, X. Wang, M. Liao, S. Li, S. Chen, D. Golberg, Y. Bando, Nanoscale 4 (2012) 6318–6324, https://doi.org/10.1039/C2NR31791E.
[52] B.J. Hansen, N. Kouklin, G. Lu, I.K. Lin, J. Chen, X. Zhang, J. Phys. Chem. C 114 (2010) 2440–2447, https://doi.org/10.1021/jp908850j.
[53] S. Li, T. Yan, X. Liu, F. Cao, X. Fang, Adv. Funct. Mater. 33 (2023) 2214533, https:// doi.org/10.1002/adfm.202214533.
[54] C. Zuo, S. Cai, Z. Li, X. Fang, Nanotechnology 33 (10) (2022) 105202, https://doi.org/10.1088/1361-6528/ac3e35.
[55] Z. Li, M.K. Joshi, J. Chen, Z. Zhang, Z. Li, X. Fang, Adv. Funct. Mater. 30 (2020) 2005291, https://doi.org/10.1002/adfm.202005291.
[56] L. Zheng, K. Hu, F. Teng, X. Fang, Small 13 (2017) 1602448, https://doi.org/10.1002/smll.201602448.
[57] T. Yan, S. Cai, Z. Hu, Z. Li, X.J. Fang, Phys. Chem. Lett. 12 (2021) 9912–9918, https://doi.org/10.1021/acs.jpclett.1c03090.